



Dislocation Density-Based Multiscale Modeling of Deformation and Subgrain Texture in Polycrystals

MEHDI HAMID^{1,2} and HUSSEIN M. ZBIB¹

1.—School of Mechanical and Materials Engineering, Washington State University, Pullman, WA 99163, USA. 2.—e-mail: mehdi.hamid@wsu.edu

In this work, a viscoplastic fast Fourier transform (FFT)-based code is combined with a continuum dislocation dynamics (CDD) framework to analyze the mechanical behavior of polycrystalline MgAZ31 material under unidirectional tensile test. A crystal plasticity formulation including the size effects through a stress/strain gradient theory, dislocation density flux among neighboring grains and grain boundary back stress field is implemented into the CDD and coupled with VPFIT for this purpose. Then, an electron backscatter diffraction-based orientation image microscopy of a sample microstructure is applied as an input to the code. The model predicts, among other things, distributions of stress, strain, mobile dislocation density, geometrically necessary dislocation and stress-strain behavior. The numerical findings are compared with experimental results, and the micromechanical behavior of the polycrystal is discussed regarding dislocation density evaluation in different stages of strain hardening.

INTRODUCTION

The microstructure and its evolution are an important physical property of any polycrystalline metallic material. It is understood that the mechanical behavior can be controlled by manipulating the microstructure of the material.¹ Thus, understanding key parameters that may control the microstructure and thus micromechanical behavior of the material may lead to better material design. This knowledge may play a vital role in developing and designing future materials with optimum properties, such as a material with low density but with higher mechanical performance. For example, by controlling the microstructure, it is possible to develop new materials with higher mechanical performance such as strength and ductility.^{1,2}

There are many studies focusing on the effect of microstructure on the mechanical behavior of polycrystalline materials. For example, FFT-based crystal plasticity research was developed by Arul Kumar et al.³ to analyze the deformation twinning in polycrystalline MgAZ31. Also, in another study⁴ a crystal plasticity model is presented for the deformation twinning and de-twinning effect along with slip deformation to account for plastic deformation of polycrystalline Mg AZ31. One of the essential

parameters in microstructural studies is the geometrically necessary dislocation (GND) distribution of the texture. The computational calculation of GND in a microstructure is analyzed and compared with experimental data in a study by Das et al.⁵ Grain size is another parameter that has a significant effect on the mechanical performance of metallic materials. The effect of this parameter is analyzed in a VPSC-based work by Shehadeh and Ayoub⁶ where a dislocation density-based crystal plasticity is developed to analyze the grain refinement of FCC polycrystals during severe plastic deformation. Also, a numerical modeling work is presented in Ref. 7 to analyze the effect of strain rate sensitivity on the mechanical behavior of polycrystalline Mg AZ31. In another study, the effect of stress relaxation and creep on lattice strain evaluation of stainless steel was analyzed experimentally and verified by elastic viscoplastic self-consistent (EVVPS) and elastic-plastic self-consistent (EPSC) models.⁷ Also, Knezevic et al.⁸ developed a multiscale model for polycrystalline metals where the elastic deformation, slip and twinning are considered in the framework. The work analyzed the tension, compression and torsion mechanical behavior of the Mg AZ31 microstructure for a wide

range of strain rates and temperatures by applying T-CPFE (Taylor-type crystal plasticity finite element).

The effect of dislocation density on twin propagation for Mg AZ31 was analyzed by Knezevic et al.⁹ by applying crystal plasticity finite element (CPFE). One of the main findings is that the increase in dislocation density content in the twinned region can lead to slower twin propagation and increase the immobile dislocation density content, which leads to an increase in hardness for Mg AZ31. In another study,¹⁰ the effect of double twin lamella on void nucleation and failure of Mg AZ31 is analyzed by using CPFE for simple tension and compression tests where it is shown that these double twin parent interfaces in the texture can lead to void nucleation.

A coupled deformation and recrystallization model is developed in Refs. 11 and 12 with GF-VPSC (grain fragmentation), which shows that the model is capable of investigating grain nucleation at grain boundaries and transition bands. The current study shows the effect of the grain boundaries and stress/strain gradient in Mg AZ31 by applying crystal plasticity equations in the VPFFT-CDD environment where, unlike VPSC, it is capable of analyzing the applied microstructure at the sub-grain level. A detailed comparison of VPFFT-CDD with the crystal plasticity-based finite element is explained in this section.

All these recent studies show the importance of microstructure evaluation, which can shed more light on understanding the mechanical behavior of polycrystalline metallic materials.

Currently, there are many modeling tools on the market to analyze the mechanical performance of samples made out of different materials. However, most of these models are not designed for analyzing polycrystalline materials based on microstructural parameters such as the dislocation density, grain boundary and size effects. Here, we develop a dislocation-based crystal plasticity model and apply it to investigate the mechanical behavior of an Mg AZ31 microstructure with HCP crystallographic structure under unidirectional tensile test. Electron backscatter diffraction (EBSD)-based orientation imaging (OIM) experimental data on the local orientation and grain morphology of polycrystalline Mg AZ31 are used as an input microstructure for the VPFFT-CDD model.

The modeling framework consists of a viscoplastic fast Fourier transform coupled with CDD (VPFFT-CDD). VPFFT is a well-known crystal plasticity model, developed by Lebensohn.^{13–16} The benefit of FFT as a mesh-free method compared with other FEM methods is that it avoids the problems caused by meshing in the modeling. The VPFFT is also an efficient alternative for FEM methods since the calculation time in the former is on the order of $N \times \log N$ based on a fast Fourier transform (FFT) algorithm, while in FEM it is on the scale of N^2 with

N being the number of discrete points in the model.¹⁴ In FFT, the stress equilibrium will be analyzed by solving differential equations for discretized points of the microstructure on a grid.¹⁷ The details on VPFFT have been published and discussed in several publications.^{15,18} In this work, the focus is on explaining the continuum dislocation density part of the work. The primary objective is to develop further understanding of the effect of microstructure-related properties such as the grain boundary back stress effect, dislocation density flux among neighboring grains and effect of stress and strain gradients on the behavior of Mg AZ31 polycrystals. The CDD formulation, including the stress/strain gradient theory, dislocation density transmission and grain boundary back stress effect, is explained in “VPFFT-CDD constitutive model” section.

This work is structured as the follows: in “VPFFT-CDD constitutive model” section to “Grain boundary back stress field” section the VPFFT-CDD constitutive model is explained by introducing the CDD methodology and combined stress/strain models, grain boundary back stress effect and dislocation density transfer among neighboring grains models. In “Implementation of the stress/strain gradient model” section, the results from VPFFT-CDD are discussed; lastly, the outcomes of the study are described in the “Conclusion” section.

VPFFT-CDD CONSTITUTIVE MODEL

The microstructure is discretized into grains and subgrain points. In this work, OIM (orientation image microscopy) is applied to discretize the EBSD (electron backscatter diffraction) image of Mg AZ31 to points. Each point in the OIM has an orientation and ID and x and y coordinate positions and a phase ID as well. An EBSD image with a size of $81 \times 74.48 \mu\text{m}$ with a step size of $0.5 \mu\text{m}$ is imported into the OIM, and a section with the size of $63.5 \times 63.5 \mu\text{m}$ with 16,384 points is cropped from the original microstructure and applied into VPFFT-CDD to model the mechanical behavior of this sample under unidirectional plane strain tension test with a strain rate of 0.1 s^{-1} . The FFT-based modeling was initially developed by Suquet and collaborators,¹⁷ later on, it was further developed by Lebensohn and coupled with the VPSC.¹⁹ In this work, the CDD model, developed by Lebensohn,¹⁷ is combined with VPFFT, developed by Lebensohn.¹⁷ The formulation in the CDD is explained below in detail, and for the formulations of VPFFT readers are referred to previous publications.^{14,15,20,21}

CONTINUUM DISLOCATION DYNAMICS (CDD) METHODOLOGY

The plastic deformation mechanism for each grain is calculated in a crystal plasticity-based routine called CDD where evaluation of physical

variables such as dislocation velocity, mobile, and immobile dislocation densities is calculated by using relations such as the Orowan and Bailey–Hirsch equations.^{19,22} For instance, the Orowan relation $\dot{\gamma}^\alpha = \rho_m^\alpha b \bar{v}_g^\alpha$ gives the relationship between the strain rate ($\dot{\gamma}^\alpha$), mobile dislocation density (ρ_m^α), Burger's vector magnitude (b) and average glide velocity (\bar{v}_g^α) on available slip planes like α , while the average dislocation glide velocity along slip system α is related to the resolved shear stress (τ^α) and a critical resolved shear stress (τ_{crss}^α) by a power law relation given in Eq. 1.

$$\bar{v}_g^\alpha = v_0 \left| \tau^\alpha / \tau_{cr}^\alpha \right|^{1/m} \text{sign}(\tau^\alpha), \quad \tau^\alpha = \sigma : \mathbf{M}^\alpha \quad (1)$$

where σ is the Cauchy stress tensor, and \mathbf{M} is the Schmid orientation tensor for slip system α . The constants v_0 and m are the reference velocity and strain rate sensitivity, respectively,^{21,23} and set as 10^{-5} and 0.05, respectively.

Also, Eq. 2 shows the relation for calculating the critical shear stress τ_{cr}^α as follows.

$$\tau_{cr}^\alpha = \tau_0^\alpha + \tau_H^\alpha + \tau_S^\alpha \quad (2)$$

where τ_0 , τ_H^α and τ_S^α are the reference shear stress or lattice friction stress, forest dislocation hardening term and calculated by the Bailey–Hirsch relation.²⁴ The last term in Eq. 2 is the size-dependent term and is calculated by applying a stress gradient theory.²⁵ The Bailey–Hirsch hardening shear stress τ_H^α is given below:

$$\tau_H^\alpha = \alpha^* b \mu \sum_{s=1}^N \Omega^{2s} \sqrt{\rho_{TS}^s} \quad (3)$$

with α^* being the Bailey–Hirsch hardening coefficient shown in Table I²⁶ for different slip planes, b the magnitude of the Burgers vector, μ the elastic shear modulus, ρ_{TS}^α the total statistically stored dislocation density SSD and Ω^{2s} the dislocation interaction matrix accounting for dislocation interactions among slip systems.^{27,28}

Pile-up of dislocations against obstacles leads to size-dependent strength. Refs. 24, 28 show that the pile-up deformation mechanism and the intensity

and distribution and intensity of the pile-up are critically dependent on the local stress gradients. To address this problem,²⁸ a stress gradient plasticity theory for non-homogenous stress conditions was developed in Refs. 28, 29. Here, a linear version of this stress gradient theory is shown by Eq. 4, which incorporates the effect of grain size.

$$\tau_S^\alpha = \frac{K}{\sqrt{L}} \left(1 + \frac{L'}{4\bar{\tau}} |\nabla \bar{\tau}| \right) \quad (4)$$

with K being the Hall–Petch parameter, L grain size, L' obstacle spacing and $\nabla \bar{\tau}$ the gradient of effective shear stress.

The total dislocation density ρ_{TS}^α is the sum of mobile (ρ_M^α) and immobile dislocation densities (ρ_I^α) in slip system α :

$$\rho_{TS}^\alpha = \rho_M^\alpha + \rho_I^\alpha \quad (5)$$

Constitutive relations for the mobile and immobile dislocation are given by:³⁰

$$\begin{aligned} \dot{\rho}_M^\alpha &= \bar{v}^\alpha \cdot \nabla \rho_M^\alpha + \alpha_1 \rho_M^\alpha v_g^\alpha / \bar{l}_g^\alpha - \alpha_2 2R_c \rho_M^\alpha \rho_M^\alpha v_g^\alpha \\ &\quad - \alpha_3 \rho_M^\alpha v_g^\alpha / \bar{l}_g^\alpha + \alpha_4 (|\tau^\alpha| / \tau_{cr}^\alpha)^r \rho_I^\alpha v_g^\alpha / \bar{l}_g^\alpha \\ &\quad + \alpha_5 \sum_{\beta=1}^N P^{\beta\alpha} \rho_M^\beta v_g^\beta / \bar{l}_g^\beta - \alpha_6 R_c \rho_M^\alpha \rho_I^\alpha v_g^\alpha \end{aligned} \quad (6)$$

$$\dot{\rho}_I^\alpha = \alpha_3 \rho_M^\alpha v_g^\alpha / \bar{l}_g^\alpha - \alpha_4 (|\tau^\alpha| / \tau_{cr}^\alpha)^r \rho_I^\alpha v_g^\alpha / \bar{l}_g^\alpha - \alpha_6 R_c \rho_M^\alpha \rho_I^\alpha v_g^\alpha \quad (7)$$

Here α_1 , α_2 , α_3 , α_4 , α_5 and α_6 are defined in Table S1. R_c is the minimum critical distance between two dislocations for mutual interaction, which is equal to $15b$, the components of $P^{\beta\alpha}$ are obtained from Monte Carlo analysis based on the probability of cross slip from β -plane to α -plane,²⁵ r is a numerical constant, and \bar{l}_g^α is the dislocation mean free path:^{31,32}

$$\bar{l}_g^\alpha = \frac{c^*}{\sqrt{\sum_{\alpha=1}^N w_j^\alpha (\rho_T^\alpha + \rho_{GND}^\alpha)}} \quad (8)$$

Table I. Applied parameters for Mg AZ31. $\alpha_2 = \alpha_3 = \alpha_6 = 1.0$ and $R_c = 25b$ for all the slip systems with the magnitude of Burgers vector set as 3.21×10^{-10} m⁴²

	Basal	Prismatic	Pyramidal	Twin
τ_0 (internal friction) (MPa)	4	11	40	20
α^* (Bailey–Hirsh hardening coefficient)	0.8	1.0	1.0	0.8
α_1	0.07	0.05	0.02	0.02
α_4	0.02	0.02	0.01	0.01
Ω	$\Omega^{\text{basal}} = 0.2$ $\Omega^{\text{Prismatic}} = 1.0$ $\Omega^{\text{Pyramidal}} = 1.0$	$\Omega^{\text{basal}} = 1.0$ $\Omega^{\text{Prismatic}} = 0.2$ $\Omega^{\text{Pyramidal}} = 1.0$	$\Omega^{\text{basal}} = 1.0$ $\Omega^{\text{Prismatic}} = 1.0$ $\Omega^{\text{Pyramidal}} = 1.0$	$\Omega^{\text{basal}} = 1.0$ $\Omega^{\text{Prismatic}} = 1.0$ $\Omega^{\text{Pyramidal}} = 1.0$
K (MPa mm ⁻²) ⁴³	0.42	3.72	4.71	3.72

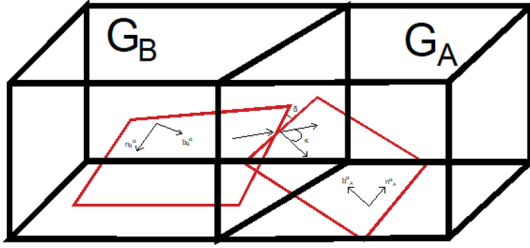


Fig. 1. Schematic representation of slip planes in grains A and B.

where c^* is a constant that is set as unity, $w^{j\alpha}$ is a simplified weight matrix as identity matrix,¹ and ρ_{GND}^α is the geometrically necessary dislocation density where its norm is given by,¹

$$\rho_{\text{GND}}^\alpha = \frac{1}{b} \sqrt{\alpha_{ij} \alpha_{ij}} \quad (9)$$

where α_{ij} is the Nye's tensor whose rate is given by the following relation.³³

$$\dot{\alpha} = \text{curl}(-\mathbf{L}^p) \quad (10)$$

with \mathbf{L}^p being the plastic part of the velocity gradient tensor.

In Eq. 6, $\nabla \rho_M^\alpha$ is the dislocation flux accounting for the transfer of dislocations across grain boundaries. Numerically, it is calculated using a central difference scheme where the difference of dislocation density across two neighboring grains is divided by some incremental distance.²⁹ For example, $\rho_M^{\alpha(A)}$ and $\rho_M^{\alpha(B)}$ are the dislocation density of grain A and B along slip system α shown in Fig. 1. In this schematic, dislocations transfer from grain B to A along the black arrow at the intersection of the two rectangular red slip planes from these two neighboring grains. It should be noted that in this work the exterior discrete points along the grain boundaries are responsible for this dislocation density transfer phenomenon.

The dislocation density transfer among neighboring grains takes place only when the stress on a slip system is more than τ_{GB}^α and when some geometrical conditions are met.^{34,35} The τ_{GB}^α is defined for each grain boundary by Eq. 11.

$$\tau_{\text{GB}}^\alpha = (1 - \lambda) \tau_{\text{max}}^\alpha \quad (11)$$

where τ_{max}^α is calculated by Eq. 13 from the stress field of dislocations in and near the grain boundary, which is explained in "Grain boundary back stress field" section. Notably, $\lambda(\phi_1, \phi, \phi_2)$ is the slip transmissivity number, which is defined by Eq. 12.³⁶ According to Ref. 35, the angle δ is the angle between slip planes and the grain boundary plane, and κ is the angle between the slip direction of slip planes shown in Fig. 1. Since it is very difficult to measure angle δ experimentally, it is suggested to apply angle ε , which is the angle between the vectors normal of the slip planes (n_A^α, n_B^α) instead of δ , i.e.,

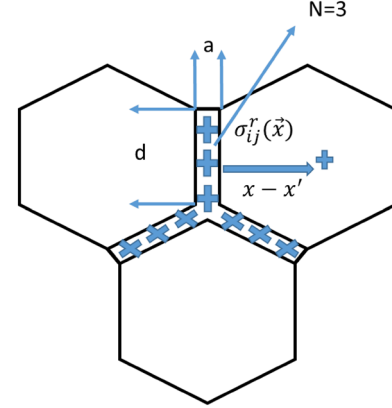


Fig. 2. A simple schematic of the dislocation interactions in an infinite homogeneous medium of the grain boundary with neighboring grains.

$$\lambda_i^\alpha = \cos\left(90 \frac{\varepsilon_i^\alpha}{\varepsilon_c^\alpha}\right) \cos\left(90 \frac{k_i^\alpha}{k_c^\alpha}\right) \quad (12)$$

where ϕ_1, ϕ, ϕ_2 are the Euler angle triplets, and ε_i^α and k_i^α are the angles among the normal of slip planes and the angle between the direction of the slip planes shown in Fig. 1 respectively. The critical values of these two angles are defined by ε_c^α and k_c^α , which are equal to 15° and 45° , respectively.³⁷ The basis for choosing these critical limits is the efficiency of slip transfer across the grain boundaries according to Ref. 29, where, for example, by increasing δ in Fig. 1 from 0° , which makes the most favorable configuration for slip transfer more than 0, which requires simultaneous initiation of dislocation loops in the neighboring grains in many parallel slip planes and leads to a significant drop in the amount of dislocation density flux. The values of ε_i^α and k_i^α should be less than their critical values in order to meet the geometrical condition mentioned previously.

GRAIN BOUNDARY BACK STRESS FIELD

The interaction among grain boundaries and dislocations in this work is modeled by using Nye's tensor.²⁸ Grain boundaries are considered as rectangular boxes filled with discrete dislocations. The length of these boundaries depends on the size of the grains. The extended stress field of each grain boundary can be calculated by applying Nye's tensor and using Mura's integral equation.²⁸ Nye's tensor represents a net dislocation density at point X' for any material that leads to long-range stress field $\sigma_{ij}^r(\vec{x})$ (Fig. 2). The stress field from each grain boundary can affect the dislocations in neighboring grains and can act as a barrier to dislocation motion. Hence, for the dislocations to pass the boundary, the resolved shear stress acting on the dislocation must also overcome the extended stress field from the

boundary. The stress field of a dislocation wall representing a grain boundary is given by the following integral equation.

$$\sigma_{ij}^r(\vec{x}) = C_{ijkl} \int_{V'} \epsilon_{lnh} C_{pqmn} G_{kp,q}(\vec{x} - \vec{x}') \alpha_{hm} dV' \quad (13)$$

where C_{ijkl} is the fourth order elasticity tensor, ϵ_{lnh} is the permutation tensor, $G_{kp,q}$ is Green's function, q signifies the spatial derivative, and $C_{pqmn} G_{kp,q}$ in the above equation for assumed isotropic elasticity in this part of the work is given by

$$C_{pqmn} G_{kp,q}(x_1 - x'_1, x_2 - x'_2, x_3 - x'_3) = \frac{-1}{8\pi(1 - \nu_1)} \left[(1 - 2\nu_1) \frac{\delta_{ni}(x_m - x'_m) + \delta_{im}(x_n - x'_n) - \delta_{mn}(x_i - x'_i)}{R^3} + 3 \frac{(x_m - x'_m)(x_n - x'_n)(x_i - x'_i)}{R^5} \right] \quad (14)$$

in which $R = \sqrt{(x_1 - x'_1)^2 + (x_2 - x'_2)^2 + (x_3 - x'_3)^2}$, and δ_{ij} is the Dirac delta function.

The Nye's dislocation density tensor²⁸ α_{hm} represents the total Burgers vectors of the m th component of all the dislocations intersecting the plane so that its normal is in the h direction. For a given set of discrete dislocations, the continuum dislocation density tensor is given by

$$\alpha_{hm} dV' = b_m \nu_h dl' \quad (15)$$

where l' and V' are the dislocation segment length and the grain boundary volume over which the dislocations are homogenized, respectively. For a set of pure edge dislocation forming a tilt wall, it can be easily shown that the only remaining component of the Nye's tensor is α_{31} , i.e.,

$$\alpha_{31} = Nb/ad \quad (16)$$

with N being the total number of dislocations; a and d are the length of wall and breadth of the homogenizing domain of the grain boundary, respectively. Figure 2 explains the parameters in Eq. 16.

Normally, the grain boundary-dislocation interactions in classical models are considered a dislocation-obstacle interaction. However, the approach in this research considers the grain boundaries as rectangular boxes filled with discrete dislocations. The length of these rectangular boxes of boundaries depends on the grain size, while the thickness of these boundaries are uniform and considered as $5b$,²⁸ which is shown schematically in Fig. 2. Then, the long-range stress field of the dislocations in each grain boundary is modeled by using Nye's tensor where Mura's integral method is applied to integrate the Nye's tensor. The maximum stress from the stress field of each boundary is assumed to be the strength of the boundary, i.e., the strength the barrier dislocations need to overcome to penetrate through the boundary.

IMPLEMENTATION OF THE STRESS/ STRAIN GRADIENT MODEL

The spatial gradients are evaluated numerically using a moving least square method strain.^{38,39} Here, the 2D microstructures are generated and coupled with the VPFFT, where each grain and sub-grain is assigned spatial coordinates. Then, the 'moving least square method' is used to evaluate the stress and strain gradient of each grain and sub-grain by using data from the nearest neighboring grains. This included the stress and strain state in each grain as calculated by VPFFT. The mathematical and numerical details about this formulation are provided by the authors.^{1,40}

RESULTS AND DISCUSSION

The model discussed above is applied to a microstructure obtained from an electron backscatter diffraction (EBSD)-based orientation image microscopy (OIM) of an HCP polycrystalline Mg AZ31. The initial dislocation density for this model was considered 10^{10} m^{-2} .⁴¹ Also, all the applied parameters in the model are shown in Table I. Figure 3a shows the undeformed EBSD-OIM Mg AZ31 microstructure that is applied to the VPFFT-CDD framework, and Fig. 3b is a grain boundary map, generated by OIM. The red lines are low-angle grain boundaries with angle ranges of 2° to 5° , where green lines are the grain boundaries with 5° to 15° , and the blue lines are high-angle grain boundaries with a $> 15^\circ$ misorientation angle. A plane strain unidirectional tensile test is conducted on this microstructure up to 25% deformation.

It is understood that plastic deformation of polycrystalline Mg AZ31 is due to active slip systems in basal planes $\{001\} \langle 110 \rangle$, prismatic planes $\{100\} \langle 110 \rangle$, pyramidal $\langle a \rangle$ planes $\{112\} \langle 110 \rangle$, pyramidal $\langle c + a \rangle$ planes $\{123\} \langle 113 \rangle$ and $\{102\} \langle 101 \rangle$ tensile twinning planes. These slip systems along with the parameters listed in Table I are applied to the modeling framework to calculate the stress, strain, mobile dislocation density and GND distribution in the applied microstructure of Mg AZ31.

Figure 4a shows the spatial stress distribution in the microstructure. The role of grain boundaries as a barrier to mobile dislocation density is examined. The stress distribution around the grain boundaries reveals the amount of stress each grain carries during the uniaxial plain strain tensile test modeling. The red spots show high-stress concentration regions in the microstructure. By comparing Figs. 3b and 4a, the effects of misorientation of grain boundaries and mobile dislocation density transfer among grains become clearer by noting that almost all the stress concentration red spots are around the high-angle boundaries.

Figure 4b shows the strain distribution in the microstructure. It is understood that the strain localization occurs at high-angle grain boundaries

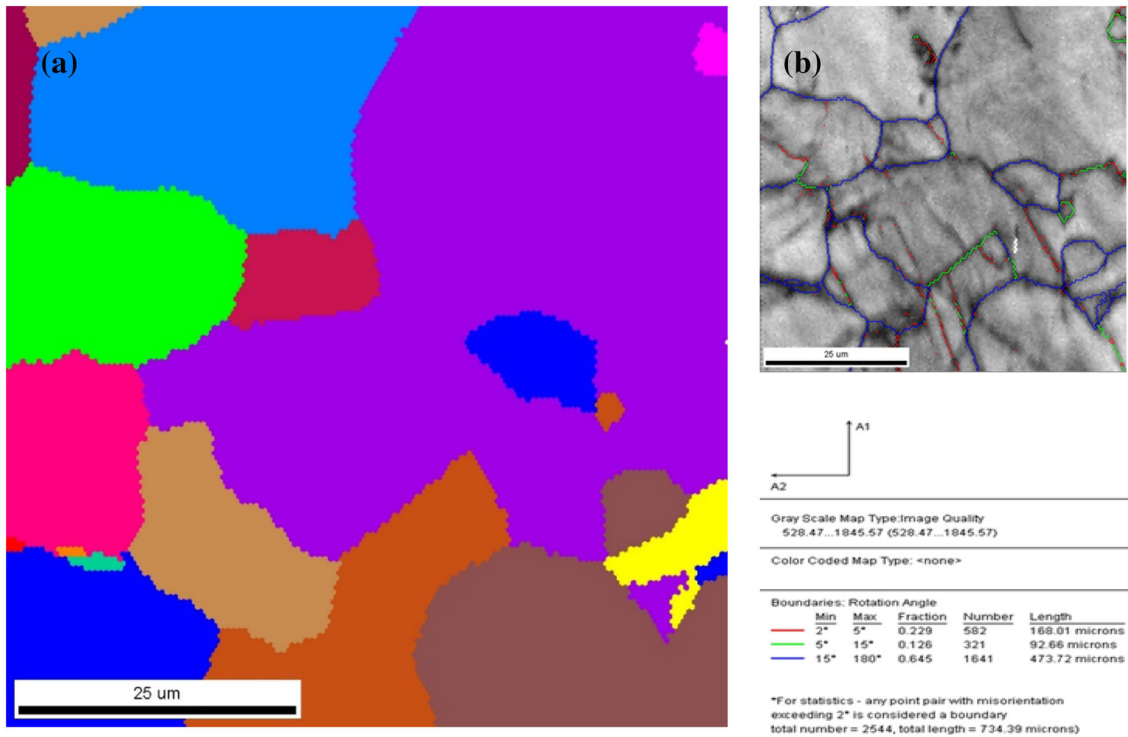


Fig. 3. (a) Grain structure used for simulations with VPFFT-CDD. (b) Grain boundary distribution in the microstructure from OIM (Color figure online).

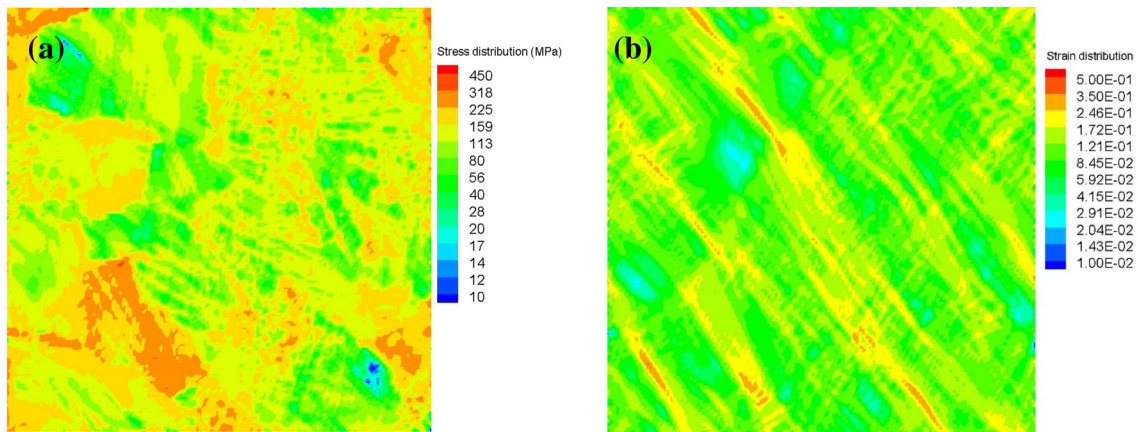


Fig. 4. (a) Stress distribution and (b) strain distribution in the microstructure (Color figure online).

where the crack initiation can occur. The red spots in Fig. 4b show the high strain localization spots of the microstructure.

The interactions of dislocations and twins are analyzed in Ref. 9. It is shown that this interaction leads to the onset of strain localization, void nucleation and crack propagation in Mg AZ31. In Fig. 4, the stress and strain localization regions are captured around high-angle grain boundaries. It should be noted this finding is in close agreement with previous studies.^{9,10}

The mobile dislocation density distribution is represented in Fig. 5. The range of mobile dislocation density is from 10^{10} to $8 \times 10^{14} \text{ m}^{-2}$. The effect of dislocation density flux is analyzed here by using the VPFFT-CDD model. Comparing Figs. 3b and 5 shows that mobile dislocation density flux occurs in most of the green and red color grain boundaries and high-angle grain boundaries kept most of the mobile dislocation densities inside the grains with blue (high-angle) boundaries.

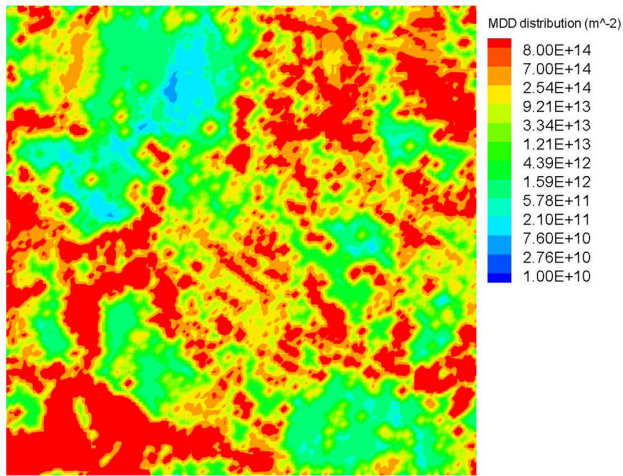


Fig. 5. Mobile dislocation density distribution of the microstructure (Color figure online).

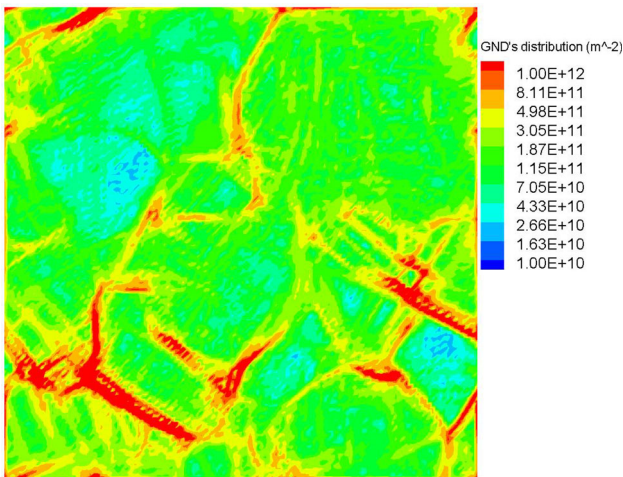


Fig. 6. GND distribution at 5% strain (Color figure online).

The GND distribution at 5% strain is shown in Fig. 6. Interestingly, almost all the grain boundaries are detected by the model, and the larger values of GNDs are distributed around the grain boundaries.

Finally, the engineering stress–strain curve is shown in Fig. 7, and the experimental data points are added to this curve to compare the modeling result with the experimental tension test for polycrystalline Mg AZ31.⁴³ The numerical results capture the overall trend of the experimental data. At the initial stage of deformation, the high rate of strain hardening is due to dislocation multiplications and interaction with boundaries. Upon further straining, the annihilation rate increases, which, in turn, decreases the rate of strain hardening.

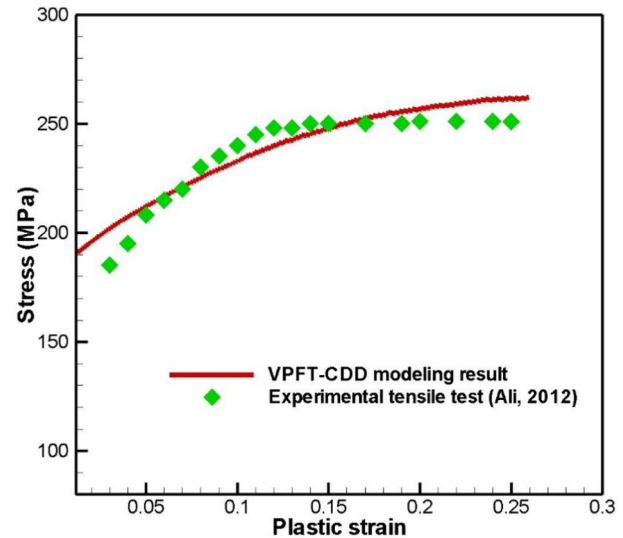


Fig. 7. Engineering stress versus strain modeling and experimental results.⁴³

Finally, the dislocation density generation and annihilation rates become balanced, and this is the cause of the very slow growth of stress values in the stress versus strain curve shown in Fig. 7.

CONCLUSION

A CDD model is coupled with VPFFT, and the spatial distribution of stress, strain, mobile dislocation density and geometrical dislocation density are analyzed based on dislocation density evaluation along known slip and twin systems for the HCP polycrystalline Mg AZ31 microstructure. The comparison of experimental and modeling stress–strain curves shows that the applied crystal plasticity relations can predict the tensile test result of this polycrystal. Also, the GND distribution map shows that the model properly captures the grain boundaries since most of the high-density GND points are around the boundaries.

ACKNOWLEDGMENTS

The support provided by the National Science Foundation's CMMI program to WSU under Grant No. 1434879 is gratefully acknowledged.

ELECTRONIC SUPPLEMENTARY MATERIAL

The online version of this article (<https://doi.org/10.1007/s11837-019-03744-w>) contains supplementary material, which is available to authorized users.

REFERENCES

1. M. Hamid, H. Lyu, and H. Zbib, *Philos Mag* 98, 2896 (2018).
2. C. Paramatmuni and A.K. Kanjarla, *Int. J. Plast* 113, 269 (2019).
3. M. Arul Kumar, I.J. Beyerlein, and C.N. Tomé, *Acta Mater.* 116, 143 (2016).
4. H. Wang, P.D. Wu, J. Wang, and C.N. Tomé, *Int. J. Plast* 49, 36 (2013).
5. S. Das, F. Hofmann, and E. Tarleton, *Int. J. Plast* 109, 18 (2018).
6. A.H. Kobaiassy, G. Ayoub, L.S. Toth, S. Mustapha, and M. Shehadeh, *Int. J. Plast* 114, 252 (2018).
7. H. Wang, B. Clausen, C.N. Tomé, and P.D. Wu, *Acta Mater.* 61, 1179 (2012).
8. M. Ardeljan, I.J. Beyerlein, B.A. McWilliams, and M. Knezevic, *Int. J. Plast* 83, 90 (2016).
9. M. Ardeljan and M. Knezevic, *Acta Mater.* 157, 339 (2018).
10. M. Ardeljan, I.J. Beyerlein, and M. Knezevic, *Int. J. Plast* 99, 81 (2017).
11. M. Zecevic, R.A. Lebensohn, R.J. McCabe, and M. Knezevic, *Int. J. Plast* 109, 193 (2018).
12. M. Zecevic, R.A. Lebensohn, R.J. McCabe, and M. Knezevic, *Acta Mater.* 164, 530 (2019).
13. A. Eghtesad, M. Zecevic, R.A. Lebensohn, R.J. McCabe, and M. Knezevic, *Comput. Mech.* 61, 89 (2018).
14. R.A. Lebensohn, R. Brenner, O. Castelnau, and A.D. Rollett, *Acta Mater.* 56, 3914 (2008).
15. R.A. Lebensohn, E.M. Bringa, and A. Caro, *Acta Mater.* 55, 261 (2007).
16. R.A. Lebensohn and A. Needleman, *J. Mech. Phys. Solids* 97, 333 (2016).
17. R.A. Lebensohn, *Acta Mater.* 49, 2723 (2001).
18. J.C. Michel, H. Moulinec, and P. Suquet, *Int. J. Numer. Meth. Eng.* 52, 159 (2001).
19. H. Askari, J. Young, D. Field, G. Kridli, D.S. Li, and H. Zbib, *Philos Mag* 94, 381 (2014).
20. H. Moulinec and P. Suquet, *Comput Method Appl M* 157, 69 (1998).
21. J.E. Bailey and P.B. Hirsch, *Philos Mag* 5, 485 (1960).
22. E. Orowan, *Proceedings of the Physical Society* 52, 8 (1940).
23. Q. Wei, L. Kecskes, T. Jiao, K.T. Hartwig, K.T. Ramesh, and E. Ma, *Acta Mater.* 52, 1859 (2004).
24. N. Taheri-Nassaj and H.M. Zbib, *Int. J. Plast* 74, 1 (2015).
25. H. Lyu, A. Ruimi, and H.M. Zbib, *Int. J. Plast* 72, 44 (2015).
26. S. Queyreau, G. Monnet, and B. Devincre, *Int. J. Plast* 25, 361 (2009).
27. D. Terentyev, D. Bacon, and Y.N. Osetsky, *J. Phys.: Condens. Matter* 20, 445007 (2008).
28. S. Akarapu and J.P. Hirth, *Acta Mater.* 61, 3621 (2013).
29. M. Hamid, H. Lyu, B.J. Schuessler, P.C. Wo, and H.M. Zbib, *Crystals* 7, 152 (2017).
30. D.S. Li, H. Zbib, X. Sun, and M. Khaleel, *Int. J. Plast* 52, 3 (2014).
31. H.T. Zhu and H.M. Zbib, *Acta Mech.* 121, 165 (1997).
32. T. Ohashi, *Int. J. Plast* 21, 2071 (2005).
33. K. Shizawa and H.M. Zbib, *Journal Of Engineering Materials And Technology-Transactions Of The Asme* 121, 247 (1999).
34. Z. Shen, R.H. Wagoner, and W.A.T. Clark, *Acta Metall.* 36, 3231 (1988).
35. K.G. Davis, E. Teghtsoonian, and A. Lu, *Acta Metall.* 14, 1677 (1966).
36. E. Werner and W. Prantl, *Acta Metall. Mater.* 38, 533 (1990).
37. J.F. Nye, *Acta Metall.* 1, 153 (1953).
38. M.G. Armentano and R.G. Duran, *Appl Numer Math* 37, 397 (2001).
39. W.K. Liu, S.F. Li, and T. Belytschko, *Comput Method Appl M* 143, 113 (1997).
40. H. Lyu, M. Hamid, A. Ruimi, and H.M. Zbib, *Int. J. Plast* 97, 46 (2017).
41. G.D. Sim, G. Kim, S. Lavenstein, M.H. Hamza, H.D. Fan, and J.A. El-Awady, *Acta Mater.* 144, 11 (2018).
42. B. Raeisinha, S.R. Agnew, and A. Akhtar, *Metallurgical and materials transactions.* 42, 1418–1430 (2011).
43. U. Ali, *Numerical Modeling of Failure in Magnesium Alloys under Axial Compression and Bending for Crashworthiness Applications.* Master Thesis, University of Waterloo (2012).

Publisher's Note Springer Nature remains neutral with regard to jurisdictional claims in published maps and institutional affiliations.